Materials Advances

ROYAL SOCIETY OF CHEMISTRY

PAPER

View Article Online
View Journal | View Issue

Cite this: *Mater. Adv.*, 2021, 2, 3353

Cobalt nanoparticle catalysed graphitization and the effect of metal precursor decomposition temperature†

Stuart J. Goldie, Shan Jiang and Karl S. Coleman *

Received 10th February 2021,
Accepted 31st March 2021

DOI: 10.1039/d1ma00125f

rsc.li/materials-advances

Porous carbon foams hold great promise for supercapacitors and next generation energy storage materials but greater control over the formation of the pore structure would aid the development of these materials. High temperature graphitization has been investigated as a sustainable method of producing these technologically important materials and the addition of transition metals is known to promote the formation of graphitic carbon and potentially control the pore structure, however the effect of different metal precursors has rarely been examined. Using different cobalt salts, specifically $Co(OAc)_2$, $CoCl_2$ and $Co(NO_3)_2$, in a dextran/TritonX-45 aerogel graphitization, the foams produced were analyzed using Raman spectroscopy, XRD, thermal analysis, gas sorption and various electron microscopy techniques. These revealed that when using salts with low thermal stability such as $Co(NO_3)_2$ and $Co(OAc)_2$ the metal nanoparticles are formed rapidly and become trapped in the carbon matrix causing uniform graphitization. In contrast, when stable salts are used such as $CoCl_2$ the carbon decomposes before metal reduction and large metal crystals, microns in size, are formed. This control of nanoparticle size through understanding the thermal stability of metal precursors should be general to other widely used reagents to inform the rational design and production of future functional materials.

Introduction

Porous carbon foams are attracting interest for important energy storage applications in battery and supercapacitor devices, as well as potential photo and electro-catalyst supports thanks to the low density, high surface area and desirable conductivities possible,[1–5] and because graphitic and amorphous carbon foams can be produced from sustainable biomass.[6] In contrast, self-assembly from graphene oxide dispersions readily produces high surface area structures but the oxidised graphene used to form the dispersion contains defects in the sp^2 carbon network reducing many of the most useful properties.[7–10] Alternatively, chemical vapour deposition onto porous templates has produced high quality few-layer graphene foams, however this requires an expensive synthesis and produces low volumes of material.[11–14]

Graphitization, the high temperature conversion of carbon materials into graphite, has been applied to porous and templated carbon materials for decades and represents a facile method of converting biomass or polymer structures into porous graphitic carbon.[15–17] Such methods have been applied to form hard carbon anodes for sodium and lithium ion batteries and supercapacitor electrodes.[18–20] The transformation of carbon into graphite is known to occur spontaneously, but only at very high temperatures often exceeding 2000 °C.[17] The presence of transition metals reduces the temperature at which this process happens thanks to dissolution/precipitation by which the carbon forms a high temperature super saturated solution in the metal (or in some cases stable metal carbide) that precipitates forming graphite crystals.[21,22] Recently there have been many attempts to produce porous graphitic materials from polymers or biomass, mixed either with metal particles or metal salts that form metals *in situ*.[17,23–27] In a study of this process Sevilla *et al.* proposed the conversion proceeded by the decomposition of the metal precursor and carbon material to produce metal, or metal oxide, nanoparticles embedded in an amorphous carbon structure; these nanoparticles then convert the surrounding carbon into graphitic crystallites.[25,28]

Many carbon based materials can in principle be graphitized but the most common approaches use: polymer xerogels from emulsion polymerization to form a polymer foam with transition metal salts dissolved in the aqueous phase;[23,25,29–32] insoluble carbon feedstocks, often biomass, into which metal salt solutions are soaked;[19,28,33–35] and solutions of both metal salts and carbon feedstock that form well mixed materials when dried.[22,26,36,37]

Department of Chemistry, Durham University, South Road, Durham, DH1 3LE, UK. E-mail: k.s.coleman@durham.ac.uk

† Electronic supplementary information (ESI) available: Thermal analysis, XRD indexing, Raman spectra, EM images and particles sizing, gas sorption and GC–MS. See DOI: 10.1039/d1ma00125f

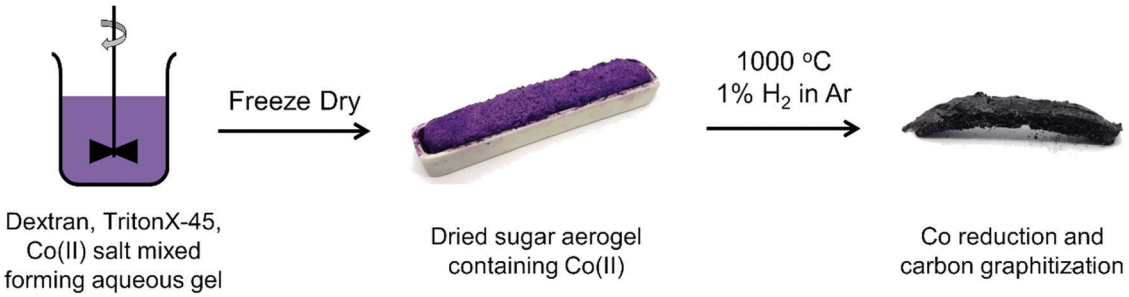

Scheme 1 Preparation of dextran and TritonX-45 gel containing Co(II) salts, photograph of dried aerogel in a recrystallised alumina crucible and a photograph of the carbonized foam after heat treatment.

The most common catalyst precursors are transition metal salts, often of Fe, Ni or Co, that decompose at elevated temperatures to form the catalytic metal.[38,39] The mixed foam is then heated under an inert atmosphere to high temperatures, usually exceeding 800 °C, causing decomposition into elemental carbon. An example of a single solution prepared from soluble sugars and cobalt salts, followed by drying and heating is shown in Scheme 1. During graphitization carbon will undergo rearrangement to adopt the hexagonal layers of graphene and graphite whilst functional groups are lost as gases, commonly CO_2, CO, H_2 and light hydrocarbons; causing the structure to shrink and pores to form.[22] The resulting graphitized foam can be washed to remove metal particles and structural templates.

Structural templates or other mechanisms for controlling the porous structure are required because energy storage devices like supercapacitors require hierarchical porous structures with both micropores (smaller than 2 nm) to provide high surface areas for charge storage, and *meso* (>2 nm, <50 nm) and macro pores (>50 nm) to allow electrolyte infiltration and diffusion.[40] Hard structural templates like zeolites and silica nanoparticles are effective at controlling the resulting porosity, although, harsh washing is generally required to remove such templates;[31,41–44] alternatively soft template polymers and biomaterials have been used that require little to no washing, however, the relationship between initial gel structure and final porous carbon is still uncertain. Recently studies using gelatin with metal salts have found the interaction between the metals and the biopolymer in the initial foaming stage can have an impact on the macro porosity and structure of the final foam.[45] The metals exhibit a change in coordination environment when mixed with gelatin complicated by the pH and temperature of gel formation. The method of foam production is also reported to be important, slow heat drying produces collapsed pores whereas freeze drying the foams rapidly, produces high surface area materials.[46]

Comparisons of different transition metals as catalysts have also been undertaken, generally Cu is found to perform poorly due to its low carbon solubility, whereas Fe, Ni and Co have comparable performance producing carbon materials with different aromatic carbon content and pore structures depending on production method.[22,23,47] To investigate the graphitization process we utilize a dextran sugar based gel previously shown to be an effective template for hard metal foams used for CVD growth with cobalt salts.[48] In contrast to other investigations we vary the cobalt salts used rather than the identity of the metal and probe the relationship between the reactive salts used and the carbon foam produced. Whilst many transition metals are effective at catalyzing graphene growth in this way, cobalt nanoparticles are interesting for other applications including water splitting electrocatalysts.[49]

Experimental

Materials

Cobalt(II) nitrate hexahydrate ACS reagent ≥ 98%, cobalt(II) acetate tetrahydrate ACS reagent ≥ 98.0%, dextran from Leuconostoc mesenteroides (average mol wt 1 500 000–2 800 000) and Triton™ X-45 were all used as purchased from Sigma Aldrich. Cobalt(II) chloride hexahydrate was used as purchased from Alfa Aesar. Pureshield argon (99.998%) and hydrogen (99.995%) were used as provided by BOC. 6 M hydrochloric acid was prepared from hydrochloric acid S.G 1.18 purchased from Fisher Scientific. Furnace tube washing and waste oil analysis was done with acetone AR (99.5%) from Fisher Scientific.

Synthesis of gel

Gels were prepared in similar fashion to Khan and Mann;[50] dextran was gently stirred into water with the salt to form a viscous liquid to which Triton™ X-45 was added and the mixture then stirred with a mechanical stirrer at 600 rpm to form a homogeneous mixture. In every case 4 g of salt was used and the other reagents were added to maintain a consistent mass ratio (1 : 2 : 2) between the cobalt metal, dextran and Triton™ respectively; water was added to keep a constant ratio (1 : 2.5) between sugar and water respectively. The wet gel was placed into an alumina boat and freeze dried (SP Scientific BenchTop Pro) for at least 24 hs at ~4 Pa to produce a hard foam.

Synthesis of graphene foam

An alumina boat containing the foam was placed inside a quartz worktube (I.D 29 mm) inside a Carbolite tube furnace (MTF 12/38/400). The system was purged with argon (800 mL min^{-1}) for 30 min then hydrogen (8.72 mL min^{-1}) was added to the flow all at atmospheric pressure; argon gas flow measured by volumetric flow meter whilst hydrogen controlled by a Brooks 5850 TR Series mass controller in totalizer mode. The furnace was heated to 1000 °C at

10 °C min^{-1} and held at this temperature for one hour before it was allowed to cool.

Extraction and washing

Both the quartz worktube and resulting carbonized foam were washed with acetone (~200 mL) to remove oily residues then vacuum filtered and air dried. The oily by-product was isolated by removal of solvent *in vacuo* and then re-dissolved in acetone (10 μL mL^{-1}) for GC–MS analysis. The carbonized foam was washed with 6 M hydrochloric acid for 42 h before being filtered through a 0.02 μm membrane and washed with copious high purity water until washings were neutral; these were diluted into one litre of high purity water using a volumetric flask for ICP elemental analysis. Before any analysis of solid material all samples were dried in a vacuum oven for at least 24 hs (60 °C, <1 mbar). A note on terminology, when a distinction must be made 'carbonized' refers to carbon/metal foams before acid washing whilst 'washed' refers to carbon post acid wash.

Characterization

Raman spectroscopy. Raman spectra were recorded with a Horiba LabRam HR Evolution using a 532 nm, 1 mW laser and a ×50 long working distance objective lens. The instrument was calibrated against the 520.7 cm^{-1} Raman signal of silicon. Washed samples were ground up and pressed into flat disks for Raman mapping to generate a significant number of points for analysis that were representative of the whole material; maps were fitted with a six order polynomial background and Lorentzian line shapes using a Python program, details published previously.[51]

Thermo-gravimetric analysis (TGA). TGA was carried out with a PerkinElmer TGA 8000 heating from ambient temperature to 1000 °C at 10 °C min^{-1} under both air and nitrogen gas flow (30 mL min^{-1}); all samples were compressed to form crude pellets. Thermal analysis with *in situ* mass spectrometry was carried out with a PerkinElmer Pyris 1 TGA heating from ambient temperature at 10 °C min^{-1} under a 100 mL min^{-1} gas flow of 5% H_2/Ar mixed speciality gas from BOC. All cobalt salts were dried under vacuum (room temperature, <1 mbar) and analysed in powder form. MS analysis used a Hiden HPR-20, initially running a full range scan to identify key peaks before the measurement was repeated scanning specific mass ranges in 5 s windows.

X-ray diffraction (XRD). Powder XRD patterns of cobalt foam samples were collected with a Bruker d8 Advance diffractometer using a Mo Kα source (λ = 0.7093 Å) operating at 50 kV and 40 mA. The foam was ground into a fine powder and packed into a 1.0 mm glass capillary which was rotated at 40 rpm during the measurement; XRD fitting was done with GSASII software using *.cif* files of hcp and ccp cobalt taken from the ICSD.[52,53]

Scanning electron microscopy (SEM). SEM images were collected with a Hitachi SU-70 FEG SEM and EDX data was collected with an Oxford Instruments EDX system (X-MaxN 50 Silicon Drift Detector), data analysed with the proprietary AZtec software. All samples were imaged uncoated at 10 kV, unless otherwise stated in the caption, and stuck onto an adhesive carbon pad.

Transmission electron microscopy (TEM). TEM images were acquired using a JEOL 2100F FEG TEM operating at 80 kV. Samples were dispersed in ethanol solution then dropped onto holey carbon on a 300 mesh copper grid. Particle sizes were measured using ImageJ software.[54]

Gas sorption analysis. Gas sorption measurements were taken using a Micromeritics ASAP 2020 nitrogen porosimeter using 1/2 inch glassware fitted with a filler rod, sealed frit and isothermal jacket. The Brunauer–Emmett–Teller (BET) model was used to calculate specific surface areas from nitrogen adsorption data at 77 K in the P/P_0 range 0.05–0.25.

Inductively coupled plasma optical emission spectroscopy (ICP-OES). ICP-OES analysis was done on a Yobin Yvon Horiba Ultima 2 instrument with a radial torch and sequential monochromator; Co ICP-OES standards (0, 100, 300, 500 ppm) were used for calibration. Six measurements were taken per sample at each wavelength (350.228 nm and 356.038 nm) and averaged to give the final measured concentration of cobalt.

Gas-chromatography–mass spectrometry (GCMS). Waste oils were analysed using a Shimadzu QP2010-Ultra; Rxi-17Sil MS column (0.15 μm × 10 m × 0.15 mm) with 0.41 mL min^{-1} helium carrier gas and a temperature gradient of 50 °C min^{-1} to 300 °C; 0.5 μL samples were injected for low resolution electrospray mass spectrometry in positive ion mode (ES +).

Results and discussion

Herein we discuss the role of different cobalt salts on the morphology and graphitization of carbon foams. Firstly, a wet dextran/TritonX^{TM}-45/cobalt gel was prepared and freeze dried to form a solid material as illustrated in Scheme 1. This was heated in a mildly reducing atmosphere to generate a carbon and metal foam and then washed with HCl to isolate the final graphene-based foam. A dextran based gel was chosen as a starting point because it is simple to produce and the high oxygen content has been linked to an even distribution of cations throughout the structure.[37,50] Acetate, chloride and nitrate cobalt salts were chosen for their availability and high water solubility.

Probing the carbon produced

The large area Raman microanalysis and powder XRD of the carbonized materials clearly show the significant effect the cobalt has; the metal free control is exclusively amorphous carbon as shown by the lack of a 2D Raman peak in Fig. 1, and a very broad XRD peak centred around 10.5°, Fig. 2.[55] In contrast the cobalt containing materials show signs of graphitic domains within the structure giving rise to the strong 002 in-plane reflection in the XRD pattern and a 2D Raman signal, attributed to the resonant scattering from the sp^2 network in graphene sheets.[56] Despite this, the carbon materials produced using different cobalt salts as catalyst precursors have different degrees of graphitization. The XRD patterns (Fig. 2) show a wide 002 reflection at 2θ = 12.2° and in the case of $CoCl_2$ a sharper reflection at a greater 2θ value, 2θ = 12.4°. Using the

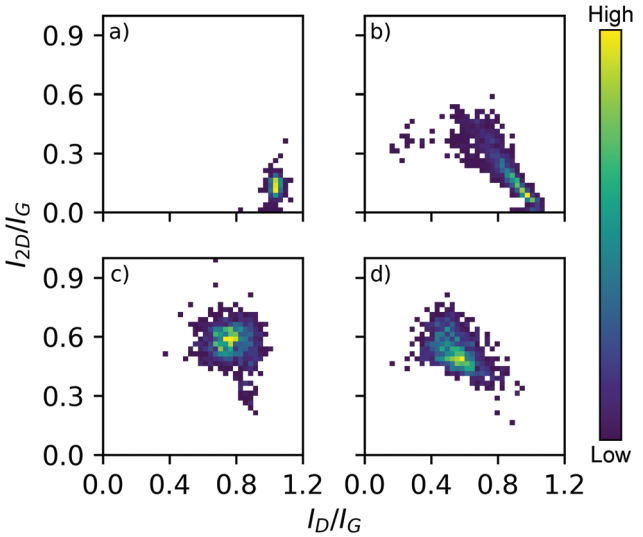

Fig. 1 3D bivariate histograms displaying Raman map data from carbonized samples derived from salts (a) metal free control, (b) $CoCl_2$, (c) $Co(OAc)_2$, (d) $Co(NO_3)_2$. Graphitic I_D/I_G and I_{2D}/I_G peak intensity ratios are on each axis and histogram frequency denoted with the heat scale shown. Representative spectra in ESI,† Fig. S12.

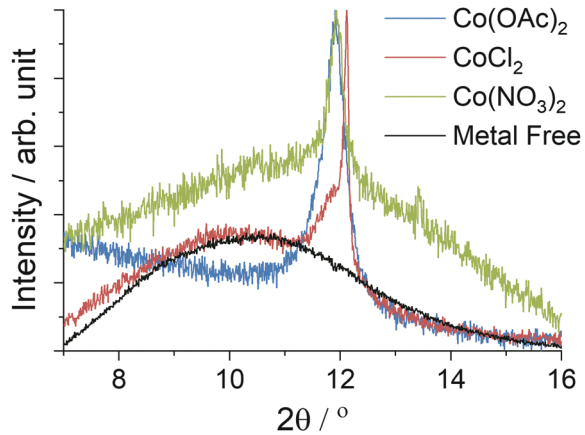

Fig. 2 Powder XRD data from the carbonized materials recorded with a Mo source (λ = 0.7093 Å), the data is the same as Fig. 4 but focused on the graphite 002 peak which appears weak due to the high metal content. Peak intensities have been normalized, whilst the metal free control is shown with reduced intensity for clarity.

graphitization models summarized by Ōya and Marsh the $CoCl_2$ derived material can be described as G-effect graphitization, in which regions of highly crystalline graphite form within an amorphous carbon structure.[57] It's also supported by the Raman map data (Fig. 1b); the amorphous carbon with a very low I_{2D}/I_G ratio but $I_D/I_G \approx 1.0$ dominates much of the map however there are points with Raman spectra more consistent with graphite, exhibiting low I_D/I_G ratios and $I_{2D}/I_G \approx 0.4$.

In contrast, the $Co(OAc)_2$ and $Co(NO_3)_2$ catalyst precursors produce materials better described by T_s-effect graphitization caused by finely divided catalyst particles that produce many turbostratic graphitic domains lacking long range 3D stacking. The XRD patterns of such materials generally have a wider 002 reflection with a 2θ value lower than the *G*-effect peak which is consistent with the observed patterns and peak position at 2θ = 12.2°. This shift of 0.2° as measured with a Mo X-ray source, while small, agrees with the reported shift of 0.5° when measured with Cu radiation (1.5406 Å).[57] A distribution of small graphitic domains is also consistent with the Raman map data (Fig. 1c and d); both $Co(OAc)_2$ and $Co(NO_3)_2$ derived foams show a I_{2D}/I_G ratio higher than expected from pristine graphite (Fig. S13, ESI†), 0.6 and 0.45 respectively but an increased I_D/I_G of 0.75 and 0.55 consistent with smaller graphite flakes.

Thermal analysis in air (Fig. S1, ESI†) reveals the $CoCl_2$ derived foam to contain two domains, one very similar to the amorphous carbon control with an onset at 580 °C and a small phase of graphitic carbon accounting for 9% of the mass that burnt at a higher temperature, onset at 650 °C. The $Co(OAc)_2$ in contrast shows only a single mass loss with an onset of 625 °C consistent with the graphitic carbon present; the $Co(NO_3)_2$ derived foam burns at a lower temperature starting at 350 °C, however this is the result of residual metal nanoparticles catalysing the combustion of the carbon surrounding them.[31]

Viewing the metal particles

Electron micrographs of the carbonized materials show very clearly the difference in metal particles produced by *in situ* reduction when using different cobalt salts. When $CoCl_2$ is used as a precursor the metal is found in large, highly crystalline particles microns in size decorated over the surface from which graphite layers can grow following the dissolution–precipitation mechanism.[21] EDX mapping (Fig. 3b) highlights the metal content concentrated exclusively into the crystals whose sharp edges and regular shapes indicate high crystallinity, a feature supported by the clear XRD pattern (Fig. 4) obtained from the carbonized material before acid washing. Further imaging after acid washing (Fig. 3c) reveals the carbon shells grown on the metal surface can actually maintain their structure even after the metal is removed from inside. Whilst it might be supposed that a complete carbon coating of the metal would protect it from reacting with the acid, the absence of any XRD diffraction peaks (Fig. S11, ESI†) or mass remaining after thermal analysis (Fig. S1, ESI†) shows that HCl etching is effective at removing the metal. The cracks and gaps observed by SEM in the carbon shell support this incomplete carbon growth from the metal that allows some acid penetration.

SEM struggles to resolve the nanoparticles present in the $Co(OAc)_2$ and $Co(NO_3)_2$ derived samples whilst the TEM images clearly show large numbers of spherical particles scattered throughout the carbon matrix (Fig. 5). These particle size distributions are shown in Fig. S17 and S18 (ESI†). Neither follow a normal distribution, instead containing a tail extending to larger particles sizes, but the $Co(NO_3)_2$ derived foam produced nanoparticles with a mean diameter of 10 ± 3 nm whilst the $Co(OAc)_2$ sample produced smaller nanoparticles 2.2 ± 0.6 nm in diameter. Larger metal particles greater than 100 nm in diameter were also observed in the $Co(NO_3)_2$ sample although they were substantially less common than the nanoparticles. These particles are observed in SEM images and EDX elemental

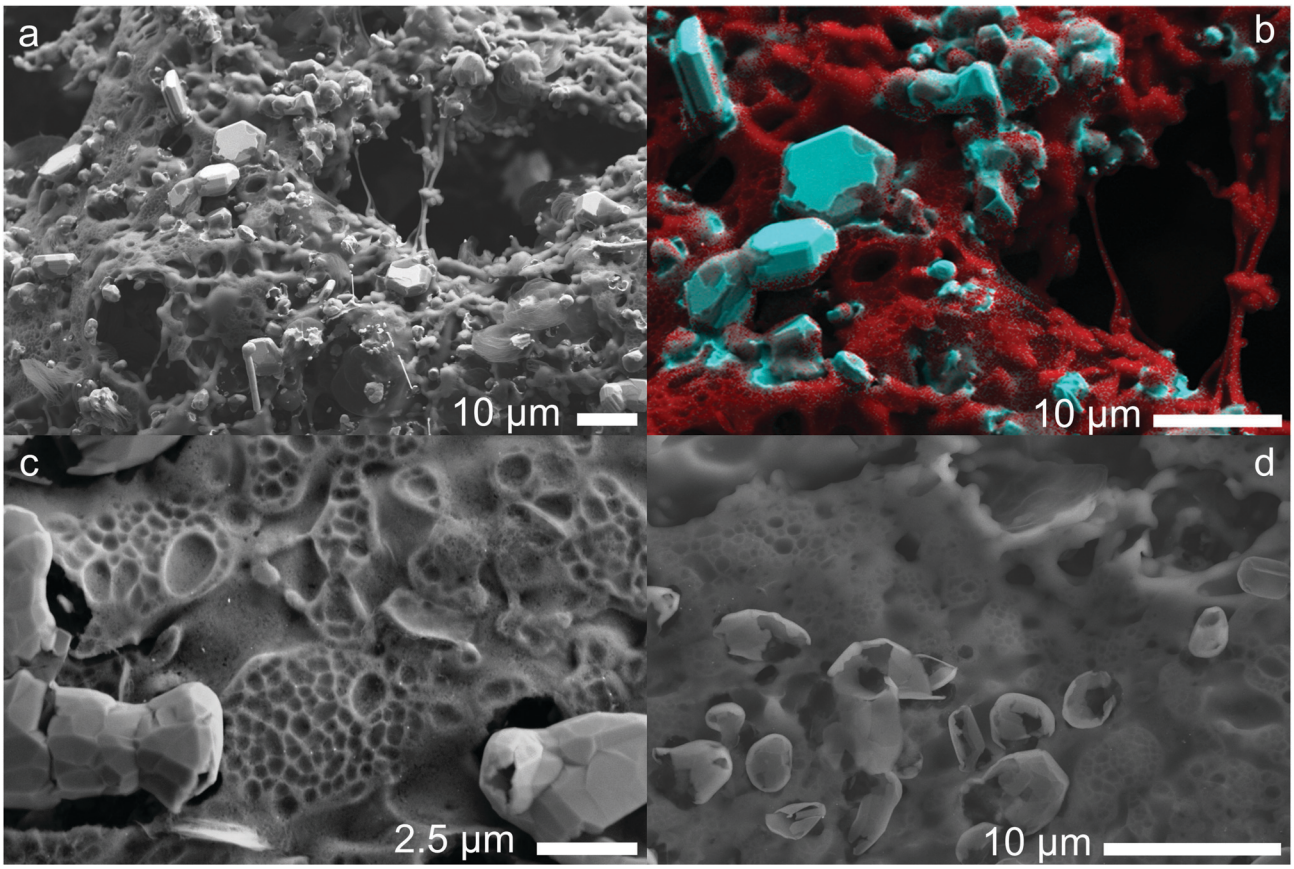

Fig. 3 Scanning electron micrographs of $CoCl_2$ derived foam after carbonization. (a) Carbonized foam before acid washing showing metal particles; (b) composite SE image and EDX map showing cobalt (blue) and carbon (red) distribution; (c) after acid washing showing carbon shells (imaged at 4 kV), a wider angle image is available in ESI;† (d) after acid washing imaged at 10 keV causing the slight transparency of the thin carbon shells.

mapping (Fig. 5b); although they are poorly resolved because the nanoparticles are smaller than the electron interaction volume at electron energy levels sufficient to excite the cobalt.

The impact of these nanoparticles on carbon graphitization has been studied and generally the same dissolution/precipitation mechanism is thought to be responsible for carbon growth, however, the significant curvature of the metal nanoparticles can induce strain in the graphite sheets or cause incomplete coverage.[21,25] The HRTEM images of the carbon around these particles and left behind after removal support these conclusions (Fig. 5d); lines are observed in circles around the particle sites indicating graphite layers grown outwards before forming a larger matrix of graphitic carbon domains crosslinked together. A selected area electron diffraction (SAED) pattern (Fig. S25, ESI†) collected from one of these regions shows clear rings with a very faint hexagonal pattern of spots visible; the spots indicate that crystalline graphite layers are present, however, there is a significant proportion of randomly oriented sheets of carbon.

Analysis of surface area

It was expected that such coverage of the metals by inert carbon would impede their removal by mineral acids. However, the foam produced from the reduction of $CoCl_2$ was not impacted due to cracks and gaps within the carbon; in contrast the $Co(NO_3)_2$ precursor formed smaller nanoparticles, some of which were completely covered by a thin layer of carbon growth. This protected some of the nanoparticles from the acid wash; there was an 8 wt% difference between the expected cobalt content and actual mass reduction following HCl washing. In addition even after acid washing metal particles were observed in the TEM images (Fig. 5d) and the thermal analysis shows a 3.8% residue at 1000 °C (Fig. S1, ESI†) and catalytic combustion at lower temperatures.[31,58] In contrast, the $Co(OAc)_2$ reduction produced very small nanoparticles that could freely migrate out of the structure; gentle dispersion in ethanol was sufficient to remove these and TEM images show the otherwise clean carbon grid decorated with metal nanoparticles.

Gas sorption analysis was performed on these materials as shown in Fig. S29 (ESI†). The small nanoparticles and porous structure of the $Co(OAc)_2$ have the highest BET surface area as measured by N_2 adsorption (Table 1), although the anomalously high reading before any washing was probably caused by removal of the nanoparticles during the sample preparation. In stark contrast the $Co(NO_3)_2$ sample had a BET surface area of 39 $m^2\ g^{-1}$ before washing but increased substantially to 103 $m^2\ g^{-1}$ despite the wash step being insufficient to removal all the nanoparticles. The smallest change upon removal of the metal was the $CoCl_2$ sample,

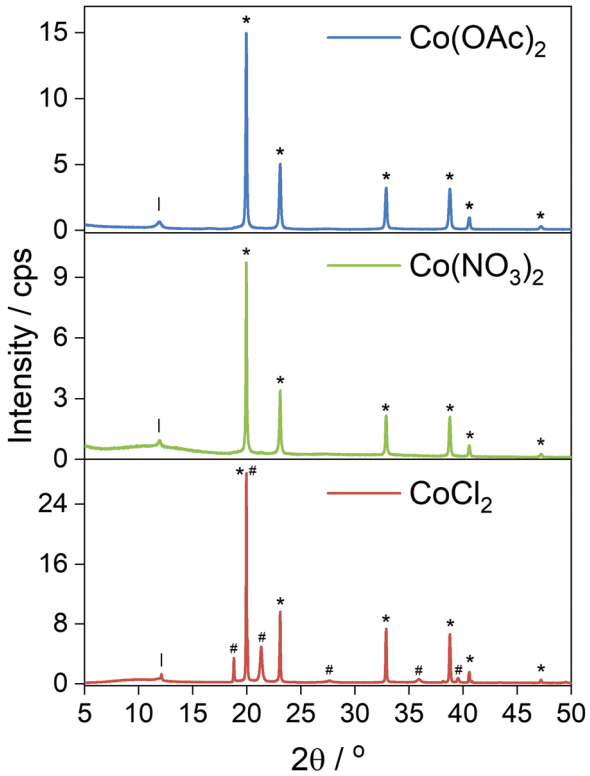

Fig. 4 Powder XRD patterns of carbonized foams containing Co metal produced *in situ*; $Co(OAc)_2$ and $Co(NO_3)_2$ salts produced metal with exclusively ccp reflections (*). The $CoCl_2$ salt produced both hcp (#) and ccp (*) phases. Full index available in ESI.†

probably due to the large particles covered in smooth graphite crystallites that will contribute less to the surface area than the amorphous regions. The N_2 isotherm shows a very significant hysteresis consistent with liquid nitrogen trapped in narrow channels by capillary forces (Fig. S29, ESI†). SEM images of the $Co(NO_3)_2$ also show regions of a more fibrous network with metal particles trapped in the carbon (Fig. S16, ESI†).

The role of different salts on the initial foaming process has been investigated and was reported to affect the macro structure of the material.[45] This effect was observed here as the $Co(NO_3)_2$ containing gel expanded to a greater volume during freeze drying than the other cobalt salt containing gels. This does not appear to have any influence on the micro-structure since the surface area for the $Co(NO_3)_2$ based foam is smaller than the other samples although the low density fibrous material seen in SEM images may be influenced by the interaction between the salt and dextran chains.

Role of metal reduction

The reduction of the cobalt salts in a hydrogen atmosphere was investigated with thermal analysis (Fig. 6) coupled to mass spectrometry; see ESI† for mass spectrometry data. $CoCl_2{\cdot}2H_2O$ is a very stable salt undergoing no significant reaction until 500 °C when it rapidly decomposes into the metal, evolving HCl as the chlorine is lost.[59] The $Co(OAc)_2$ undergoes a two-step reduction beginning at 250 °C, evolving CO_2 as the temperature increases before only the metal remains. $Co(NO_3)_2$ is the least stable salt first melting at 55 °C and losing the water of hydration; at 165 °C the nitrogen begins to decompose *via* NO_x species to leave the metal mostly reduced at 400 °C.[60]

The presence of reactive gases generated inside the foam material may explain some of the morphology observed. Significant concentrations of oxidizing NO_x gases from the $Co(NO_3)_2$ may effectively etch some of the carbon leaving a more open structure as observed with SEM and explaining the much smaller increase in percentage carbon content (Table 2). This release of gases would be expected before graphitization could occur, producing the open macroporous structure; but with individual nanoparticles later trapped by graphitization. In contrast, the CO_2 and related by-products from the $Co(OAc)_2$ do not cause additional mass loss when compared with the salt free control and the SEM shows a more dense, solid structure at low magnification levels (Fig. S14, ESI†).

The carbon produced from the $CoCl_2$ precursor is the heaviest of those measured, however, neither thermal analysis (Fig. S2, ESI†) nor EDX spectra (Fig. S28, ESI†) reveal any chlorine remaining in the carbon foam to account for this greater mass. GC–MS analysis of the oily by-products revealed significant quantities of TritonX™ fragments including many that had undergone nucleophilic substitution with the reactive HCl present (see ESI† information). However, it is worth noting that even tightly bound into clay structures, TritonX™ is known to completely desorb and vaporize by 500 °C.[61] This suggests the TritonX™ vapours condensed on the cold quartz tube outside the furnace hot zone and then HCl gas flowing from the reduction of the $CoCl_2$ reacted with the alcohol groups to produce the compounds observed, and the different masses remaining do indeed reflect the different quantities of carbon remaining after graphitization.

Given the limited evidence for the direct reaction of gases produced from the decomposition of the cobalt salts with the carbon foam, we suggest the temperature of reduction and carbon environment influences the size and distribution of the metal nanoparticles produced; and thus these nanoparticles are the key to determining the graphitization process that follows at higher temperatures.

Considering the carbon foam produced with $CoCl_2$ as a catalyst precursor, previous studies suggest that sugar based carbon undergoes pyrolysis into amorphous carbon between 300–600 °C which would be before any of the salt underwent reduction.[36,37] It follows that this would produce an open pore structure of amorphous carbon that allows significant migration of the cobalt at high temperature to anneal into micron sized crystalline particles. These large particles then graphitize the carbon around them in a highly ordered manner leaving more disordered carbon in the rest of the structure, consistent with the G model of catalytic graphitization and the characterization completed in this study.

The $Co(OAc)_2$ and $Co(NO_3)_2$ salts both decompose at lower temperatures when the carbon foam will still contain many functional groups and retain much of its original structure. The large number of oxygen functional groups may aid in evenly

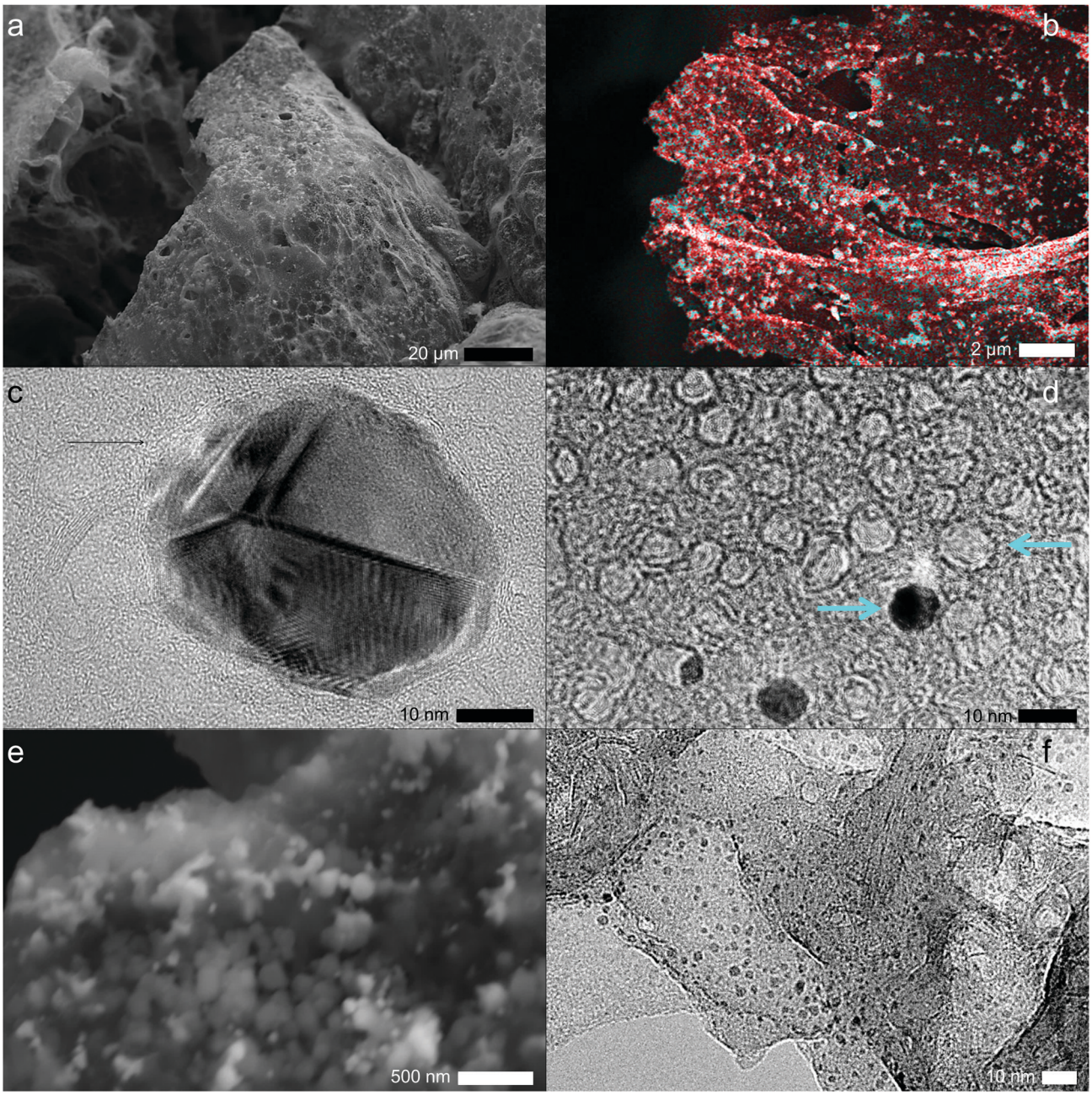

Fig. 5 Electron micrographs of the carbonized foams produced from the $Co(NO_3)_2$ (a–d) and $Co(OAc)_2$ (e and f) salts. (a) SEM with metal present, (b) composite secondary electron image and EDX map showing cobalt (blue) and carbon (red) distribution, (c) HRTEM image of a single metal particle with carbon growth visible around the edge, (d) HRTEM image after washing showing nanoparticles and the vacant sites left by other particles highlighted with arrows, (e) SEM image of carbon surface with metal present, (f) TEM of carbon sheets with nanoparticle observed on the surface.

Table 1 BET surface areas of the different foams produced from carbonization and the same foams after washing in HCl, fitted with BET model from nitrogen adsorption data

	Surface area/m^2 g^{-1}	
Cobalt precursor	Carbon & metal	Acid washed
$Co(OAc)_2$	96	144
$CoCl_2$	52	96
$Co(NO_3)_2$	39	103

dispersing the cobalt salt which, combined with the regular structure, results in localized nanoparticles that are trapped inside the carbon matrix and mostly unable to anneal into larger particles. This hypothesis is fully consistent with the microscopy and XRD data collected and would cause the T_s model graphitization observed from these samples. In a previous study with polymer aerogels Fu *et al.* found that cobalt nanoparticles began forming from $Co(NO_3)_2$ ion exchanged into a charged polymer matrix at 450 °C but carbon layers were

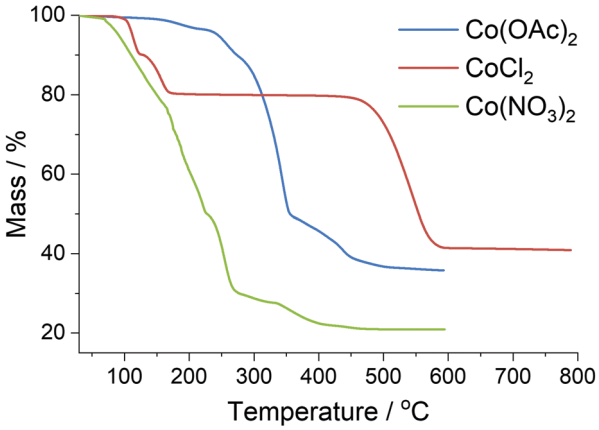

Fig. 6 Thermal analysis of metal salts used in preparation of carbon foams, completed in a reducing atmosphere.

Table 2 Solid residue = all dried, solid material after carbonization; carbon wt% before heat calculated from stoichiometry; carbon wt% after heat derived from mass remaining after acid wash to remove metal content

Sample	Solid residue wt%	Carbon wt% before heat	Carbon wt% after heat
Control	10.865(4)		
$Co(OAc)_2$*	24.610(2)	32.7(4)	40.61(4)
$CoCl_2$	28.934(3)	35.4(3)	44.69(9)
$Co(NO_3)_2$	17.799(3)	30.9(4)	32.09(9)

*Carbon content of OAc ligand not included.

not observed until 600 °C.[25] Whilst the carbon structure's interactions with the charged cobalt cations are very different between our materials, the finding of different temperatures influencing nanoparticle formation is clearly significant.

The difference between the $Co(NO_3)_2$ and $Co(OAc)_2$ salts can be explained by a mixture of temperature and reactive gas formation: the lower temperature melt and decomposition of the $Co(NO_3)_2$ followed by etching of the carbon matrix by NO_x allows the cobalt to coalesce to a greater extent forming larger nanoparticles within the structure. The $Co(OAc)_2$ in contrast does not have this space and the metal becomes trapped in very small nanoparticles distributed throughout the structure, close enough together that channels form between them after graphitization of the surrounding carbon. The larger particles from $Co(NO_3)_2$ appear to be large enough for more complete local graphitization completely enveloping the nanoparticles, protecting them from solvent and acid extraction. In both cases however, graphene formation is relatively uniform throughout the macrostructure on account of the regular presence of cobalt nanoparticles, although the highly curved surface of the nanoparticle produced strained graphene sheets with the significant I_D/I_G ratio observed.[56]

Conclusions

Mesoporous graphene foams have been produced in a single step reduction of dextran, TritonX-45™ and three common cobalt salts. The cobalt salts are shown to reduce *in situ* to form catalytic cobalt nanoparticles, and the temperature of this reduction could be used to control the graphitization and morphology of the resulting foam. This could be applicable to the production of graphitic foams for use in energy storage devices, where the compromise between high surface area carbon and more ordered graphitic regions is key. Salts that undergo reduction at low temperatures like $Co(OAc)_2$ and $Co(NO_3)_2$ are shown to form crystalline nanoparticles, trapped within the carbon structure. These cause uniform graphene growth throughout the material and template porous voids around themselves that can be accessed by removing the metal. More thermally stable salts like $CoCl_2$ only form the catalytic metal particles after the carbon support has decomposed around them, leaving large void spaces that allow for larger crystalline particles. These are very effective at graphite growth in close proximity but leave amorphous carbon in much of the structure.

Abbreviations

BET, Brunauer, Emmett, and Teller adsorption model; ccp, cubic close packed; EDX, energy dispersive X-ray spectroscopy; GC–MS, gas chromatography–mass spectrometry; hcp, hexagonal close packed; HRTEM, high resolution transmission electron microscopy; SAED, specific area electron diffraction; SEM, scanning electron microscopy; TEM, transmission electron microscopy; TGA, thermal gravimetric analysis; XRD, X-ray diffraction.

Throughout 'foam' is used to refer to a porous 3D structure of solid material separated by open void spaces irrespective of production method.

Conflicts of interest

There are no conflicts to declare.

Acknowledgements

This work was supported by a grant from the Engineering and Physical Sciences Research Council (EPSRC), UK (Ref number EP/N509462/1). This research used the GJ Russell Microscopy Facility at Durham University and the authors wish to thank Mr L. Bowen and Dr B. Mendis for their assistance with electron microscopy.

Notes and references

1 D. A. C. Brownson and C. E. Banks, *Phys. Chem. Chem. Phys.*, 2012, **14**, 8264–8281.
2 C. Xu, B. Xu, Y. Gu, Z. Xiong, J. Sun and X. S. Zhao, *Energy Environ. Sci.*, 2013, **6**, 1388.
3 N. Zhang, M.-Q. Yang, S. Liu, Y. Sun and Y.-J. Xu, *Chem. Rev.*, 2015, **115**, 10307–10377.
4 V. Kumar, K.-H. Kim, J.-W. Park, J. Hong and S. Kumar, *Chem. Eng. J.*, 2017, **315**, 210–232.
5 L. Jiang and Z. Fan, *Nanoscale*, 2014, **6**, 1922–1945.
6 Y. Li, Y. Lu, Q. Meng, A. C. S. Jensen, Q. Zhang, Q. Zhang, Y. Tong, Y. Qi, L. Gu, M.-M. Titirici and Y.-S. Hu, *Adv. Energy Mater.*, 2019, **9**, 1902852.

7 M. T. H. Aunkor, I. M. Mahbubul, R. Saidur and H. S. C. Metselaar, *RSC Adv.*, 2016, **6**, 27807–27828.
8 K. Hu, X. Xie, T. Szkopek and M. Cerruti, *Chem. Mater.*, 2016, **28**, 1756–1768.
9 L. Stobinski, B. Lesiak, A. Malolepszy, M. Mazurkiewicz, B. Mierzwa, J. Zemek, P. Jiricek and I. Bieloshapka, *J. Electron Spectrosc. Relat. Phenom.*, 2014, **195**, 145–154.
10 S. Pei and H.-M. Cheng, *Carbon N. Y.*, 2012, **50**, 3210–3228.
11 Z. Chen, W. Ren, L. Gao, B. Liu, S. Pei and H.-M. Cheng, *Nat. Mater.*, 2011, **10**, 424–428.
12 K. Chen, L. Shi, Y. Zhang and Z. Liu, *Chem. Soc. Rev.*, 2018, **47**, 3018–3036.
13 S. Drieschner, M. Weber, J. Wohlketzetter, J. Vieten, E. Makrygiannis, B. M. Blaschke, V. Morandi, L. Colombo, F. Bonaccorso and J. A. Garrido, *2D Mater.*, 2016, **3**, 45013.
14 L. Shi, K. Chen, R. Du, A. Bachmatiuk, M. H. Rümmeli, K. Xie, Y. Huang, Y. Zhang and Z. Liu, *J. Am. Chem. Soc.*, 2016, **138**, 6360–6363.
15 R. W. Pekala and C. T. Alviso, *MRS Online Proc. Libr.*, 1992, **270**, 3.
16 S. Jun, S. H. Joo, R. Ryoo, M. Kruk, M. Jaroniec, Z. Liu, T. Ohsuna and O. Terasaki, *J. Am. Chem. Soc.*, 2000, **122**, 10712–10713.
17 F. J. Maldonado-Hódar, C. Moreno-Castilla, J. Rivera-Utrilla, Y. Hanzawa and Y. Yamada, *Langmuir*, 2000, **16**, 4367–4373.
18 M. Zhong, J. Yan, H. Wu, W. Shen, J. Zhang, C. Yu, L. Li, Q. Hao, F. Gao, Y. Tian, Y. Huang and S. Guo, *Fuel Process. Technol.*, 2020, **198**, 106241.
19 D. Sun, X. Yu, X. Ji, Z. Sun and D. Sun, *J. Alloys Compd.*, 2019, **805**, 327–337.
20 K. Wang, Y. Cao, X. Wang, P. R. Kharel, W. Gibbons, B. Luo, Z. Gu, Q. Fan and L. Metzger, *Energy*, 2016, **101**, 9–15.
21 F. J. Derbyshire, A. E. B. Presland and D. L. Trimm, *Carbon N. Y.*, 1975, **13**, 111–113.
22 Q. Yan, J. Li, X. Zhang, E. B. Hassan, C. Wang, J. Zhang and Z. Cai, *J. Nanopart. Res.*, 2018, **20**, 223.
23 W. Kiciński, M. Bystrzejewski, M. H. Rümmeli and T. Gemming, *Bull. Mater. Sci.*, 2014, **37**, 141–150.
24 F. Su, J. Zeng, X. Bao, Y. Yu, J. Y. Lee and X. S. Zhao, *Chem. Mater.*, 2005, **17**, 3960–3967.
25 R. Fu, T. F. Baumann, S. Cronin, G. Dresselhaus, M. S. Dresselhaus and J. H. Satcher, *Langmuir*, 2005, **21**, 2647–2651.
26 Q. Yan, J. Li, X. Zhang, J. Zhang and Z. Cai, *Nanomater. Nanotechnol.*, 2018, **8**, 184798041881895.
27 C. J. Thambiliyagodage, S. Ulrich, P. T. Araujo and M. G. Bakker, *Carbon N. Y.*, 2018, **134**, 452–463.
28 M. Sevilla, C. Sanchís, T. Valdés-Solís, E. Morallón and A. B. Fuertes, *J. Phys. Chem. C*, 2007, **111**, 9749–9756.
29 T. Hyeon, S. Han, Y.-E. Sung, K.-W. Park and Y.-W. Kim, *Angew. Chem., Int. Ed.*, 2003, **42**, 4352–4356.
30 S. Han, Y. Yun, K.-W. Park, Y.-E. Sung and T. Hyeon, *Adv. Mater.*, 2003, **15**, 1922–1925.
31 A.-H. Lu, W.-C. Li, E.-L. Salabas, B. Spliethoff and F. Schüth, *Chem. Mater.*, 2006, **18**, 2086–2094.
32 J. Yuan, C. Giordano and M. Antonietti, *Chem. Mater.*, 2010, **22**, 5003–5012.
33 Y. Liu, Y. Guan and K. Zhang, *J. Anal. Appl. Pyrolysis*, 2019, **138**, 196–202.
34 S. Glatzel, Z. Schnepp and C. Giordano, *Angew. Chem., Int. Ed.*, 2013, **52**, 2355–2358.
35 G. Zhong, L. Ma, C. Yan, P. Zhuang and X. Ma, *Chem. Eng. J.*, 2020, **398**, 125545.
36 M. Sevilla, C. Sanchís, T. Valdés-Solís, E. Morallón and A. B. Fuertes, *Carbon N. Y.*, 2008, **46**, 931–939.
37 M. Sevilla and A. B. Fuertes, *Mater. Chem. Phys.*, 2009, **113**, 208–214.
38 A. Ōya and S. Ōtani, *Carbon N. Y.*, 1979, **17**, 131–137.
39 W. Weisweiler, N. Subramanian and B. Terwiesch, *Carbon N. Y.*, 1971, **9**, 755–761.
40 T. Liu, F. Zhang, Y. Song and Y. Li, *J. Mater. Chem. A*, 2017, **5**, 17705–17733.
41 W. Chen, S. Li, C. Chen and L. Yan, *Adv. Mater.*, 2011, **23**, 5679–5683.
42 Y. Li, K. Yan, H.-W. Lee, Z. Lu, N. Liu and Y. Cui, *Nat. Energy*, 2016, **1**, 15029.
43 *PCT Int. Appl.*, The Regents of the University of California, USA, 2017, p. 20.
44 Z. Ma, T. Kyotani and A. Tomita, *Chem. Commun.*, 2000, 2365–2366.
45 A. E. Danks, M. J. Hollamby, B. Hammouda, D. C. Fletcher, F. Johnston-Banks, S. E. Rogers and Z. Schnepp, *J. Mater. Chem. A*, 2017, **5**, 11644–11651.
46 Z. Schnepp, M. Thomas, S. Glatzel, K. Schlichte, R. Palkovits and C. Giordano, *J. Mater. Chem.*, 2011, **21**, 17760–17764.
47 J. Hoekstra, A. M. Beale, F. Soulimani, M. Versluijs-Helder, J. W. Geus and L. W. Jenneskens, *J. Phys. Chem. C*, 2015, **119**, 10653–10661.
48 M. K. Tynan, D. W. Johnson, B. P. Dobson and K. S. Coleman, *Nanoscale*, 2016, **8**, 13303–13310.
49 S.-X. Guo, Y. Liu, A. M. Bond, J. Zhang, P. Esakki Karthik, I. Maheshwaran, S. Senthil Kumar and K. L. N. Phani, *Phys. Chem. Chem. Phys.*, 2014, **16**, 19035–19045.
50 F. Khan and S. Mann, *J. Phys. Chem. C*, 2009, **113**, 19871–19874.
51 S. J. Goldie, S. Bush, J. A. Cumming and K. S. Coleman, *ACS Appl. Nano Mater.*, 2020, **3**, 11229–11239.
52 B. H. Toby and R. B. Von Dreele, *J. Appl. Crystallogr.*, 2013, **46**, 544–549.
53 E. A. Owen and D. M. Jones, *Proc. Phys. Soc., London, Sect. B*, 1954, **67**, 456.
54 C. A. Schneider, W. S. Rasband and K. W. Eliceiri, *Nat. Methods*, 2012, **9**, 671.
55 Z. Q. Li, C. J. Lu, Z. P. Xia, Y. Zhou and Z. Luo, *Carbon N. Y.*, 2007, **45**, 1686–1695.
56 A. C. Ferrari and D. M. Basko, *Nat. Nanotechnol.*, 2013, **8**, 235–246.
57 A. Ōya and H. Marsh, *J. Mater. Sci.*, 1982, **17**, 309–322.
58 J. W. Long, M. Laskoski, T. M. Keller, K. A. Pettigrew, T. N. Zimmerman, S. B. Qadri and G. W. Peterson, *Carbon*, 2010, **48**, 501–508.
59 J. R. Partington and R. P. Towndrow, *Trans. Faraday Soc.*, 1939, **35**, 553–559.
60 T. Cseri, S. Békássy, G. Kenessey, G. Liptay and F. Figueras, *Thermochim. Acta*, 1996, **288**, 137–154.
61 C. Breen, G. Thompson and M. Webb, *J. Mater. Chem.*, 1999, **9**, 3159–3165.